Journal of Materials Chemistry C

ROYAL SOCIETY OF CHEMISTRY

PAPER

View Article Online
View Journal | View Issue

Cite this: J. Mater. Chem. C, 2026, 14, 6458

An energy-efficient NbO_x/ZrO_2 bilayer memristor enabling low-voltage multilevel switching for neuromorphic computing

Muhammad Wajid Zulfiqar,[abc] Sobia Nisar,[c] Rimsha Zulfiqar,[d] Muneeb Ahmad,[bc] Muhammad Rabeel,[b] Hammad Ghazanfar,[bc] Saikh Mohammad Wabaidur,[e] Aamir Rasheed,[f] Honggyun Kim,[b] Ghulam Dastgeer *[g] and Deok-kee Kim *[bc]

The rapid growth of artificial intelligence (AI) and edge computing has intensified an urgent demand for energy-efficient hardware capable of mimicking the parallel processing and adaptive learning functions of the human brain. Memristive devices have emerged as promising candidates due to their ability to emulate synaptic behavior while offering scalability, non-volatility, and low power consumption. Despite significant progress, achieving stable low-voltage operation together with long-term reliability remains a key challenge. Here, we report the fabrication and comprehensive evaluation of a Pt/NbO_x/ZrO_2/Ag bilayer memristor that combines low-voltage switching with high reliability. Structural analyses reveal a well-defined NbO_x/ZrO_2 interface, smooth surface morphology, and clear chemical partitioning, providing a robust platform for controlled filament evolution. The device exhibits reliable resistive switching with a SET voltage of ~0.23 V, excellent endurance, stable data retention, and a large ON/OFF ratio exceeding 10^4. Tunable multilevel conductance states are achieved through compliance current modulation, as confirmed by the stable and reproducible switching characteristics. Beyond memory functionality, the bilayer architecture enables accurate emulation of key synaptic behaviors, including long-term potentiation (LTP), long-term depression (LTD), and paired-pulse facilitation (PPF). When implemented in an artificial neural network, the device achieves a recognition accuracy of ~80% on the Fashion-MNIST dataset, highlighting its potential for neuromorphic computing. These results establish the NbO_x/ZrO_2 bilayer memristor as a promising materials-engineered platform for next-generation non-volatile memory and brain-inspired computing systems with enhanced energy efficiency and scalability.

Received 15th November 2025,
Accepted 6th February 2026

DOI: 10.1039/d5tc04061b

rsc.li/materials-c

1. Introduction

The ever-increasing demand for high-performance computing and more efficient data processing, particularly in artificial intelligence (AI) and machine learning, has brought to the forefront the inherent limitations of the conventional von-Neumann architecture. The physical separation between processor and memory units creates a memory bottleneck, which results in substantial energy consumption and increased latency during data transfer between these physically distinct components.[1–3] This bottleneck becomes more pronounced as data-intensive applications demand faster and more efficient processing, highlighting the need for alternative computing architectures that integrate memory and logic more closely. The huge data explosion of asynchronous data, often referred to as "big data", flowing across various sectors, such as healthcare, education, commerce *etc.*, underscores the urgent need for more efficient and advanced systems to store and process these vast amounts of datasets.[4,5] Biological cells, particularly human neurons, are the most advanced computing units that offer remarkable parallelism and extraordinarily low energy consumption. Unlike conventional digital processors that execute instructions sequentially, the brain processes information through a vast network of highly interconnected neurons and synapses operating in parallel, consuming only about 20 watts of power.[6–8] This inherent efficiency and the ability to learn and adapt through synaptic plasticity make biological neural networks

[a] Department of Optical Engineering, Sejong University, Seoul 05006, Republic of Korea
[b] Department of Semiconductor Systems Engineering, Sejong University, Seoul 05006, Republic of Korea. E-mail: deokkeekim@sejong.ac.kr
[c] Department of Electrical Engineering and Convergence Engineering for Intelligent Drone, Sejong University, Seou 05006, Republic of Korea
[d] Department of Chemistry, Riphah International University, Faisalabad 44000, Pakistan
[e] Department of Chemistry, College of Science, King Saud University, P.O. Box 2455, Riyadh 11451, Saudi Arabia
[f] Department of Chemistry, University of Ulsan, Ulsan 44610, Republic of Korea
[g] Department of Physics and Astronomy, Sejong University, Seoul 05006, Republic of Korea. E-mail: gdastgeer@sejong.ac.kr

a compelling blueprint for next-generation neuromorphic computing. Inspired by the brain's ability to process information in parallel while seamlessly integrating memory and computation, neuromorphic computing has gained significant research interest as a transformative approach for building efficient and brain-like hardware systems.[9,10] By mimicking the brain's highly interconnected and parallel architecture, neuromorphic systems promise to significantly reduce energy consumption associated with data movement and enable real-time processing of complex, unstructured data, which is crucial for advanced AI applications.[11–14] The advancement of efficient neuromorphic systems relies fundamentally on the creation of novel electronic devices capable of replicating both synaptic plasticity and memory storage behaviors.[15,16] Memristors (memory + resistors) have attracted significant attention due to their non-volatile resistance switching behavior, which can be continuously modulated by applied electrical stimuli.[17–19] This analog and history-dependent conductance modulation makes memristors ideal candidates for artificial synapses, enabling in-memory computing and highly parallel neural network implementations. Their low power consumption, as they operate by changing resistance states rather than constantly moving charge; analog switching capabilities, allowing for a continuum of resistance states that can mimic the varying synaptic weights in biological brains, enabling more efficient learning algorithms; and excellent scalability, as they can be fabricated at nanoscale dimensions and integrated into high-density crossbar arrays, pave the way for compact and powerful neuromorphic hardware.[20–22] While single-layer memristors have shown significant potential, recent research has increasingly focused on bilayer and multi-layer structures. Despite their considerable promise, the large-scale deployment of memristive devices in neuromorphic architecture remains constrained by inherent material non-idealities. Single-layer oxide-based resistive switching devices, including ZrO_2-based systems, commonly suffer from stochastic and poorly controlled conductive filament formation. This intrinsic randomness results in degraded device-to-device uniformity, limited endurance, and most critically, nonlinear and asymmetric conductance modulation, which adversely affects synaptic weight accuracy in neuromorphic computing applications.[23–25] While single-layer NbO_x-based memristors are well known for their excellent endurance and ultrafast resistive switching behavior, they are promising candidates for high-speed neuromorphic applications. However, their practical implementation is often challenged by the relatively high operating voltages required to trigger and maintain resistive switching, which increase power consumption and hinder device scalability. In addition, the predominantly abrupt nature of filament formation and rupture in NbO_x-based systems limits the number of stable and controllable analog conductance states, thereby affecting the linearity and precision of synaptic weight modulation in large-scale neuromorphic architectures.[26,27] To address these inherent material limitations, this work employs a bilayer engineering strategy designed to simultaneously enhance device stability, improve conductance linearity and enable low-power switching suitable for scalable neuromorphic computing.[28,29] These heterostructures provide enhanced control over filament formation and rupture processes, improved switching uniformity, increased endurance, and the ability to tailor device characteristics by combining the unique properties of different materials.[30–32] Interface engineering in bilayer structures leads to more stable and predictable switching mechanisms, which are essential for achieving reliable and consistent operation in neuromorphic hardware due to temporal variations in memristor devices.[33] Transition metal oxides are particularly attractive for memristive devices due to their versatile electrical properties and compatibility with existing complementary metal–oxide semiconductor (CMOS) fabrication processes. These devices can be built directly above CMOS layers in monolithic 3D integration and incorporated into fan-out wafer-level packaging (FOWLP) and silicon interposers without the need for new manufacturing infrastructure.[34,35] This compatibility greatly facilitates their adoption in advanced packaging strategies aimed at increasing system density and performance. Both niobium oxide (NbO_x) and zirconium dioxide (ZrO_2) have demonstrated excellent memristive behavior. The oxygen vacancy-mediated switching mechanism and multi-resistance states of NbO_x make it highly suitable for implementing analog synaptic functions.[36,37] ZrO_2 offers a high dielectric constant and robust resistive switching performance, attributed to the formation and rupture of conductive filaments. These properties make NbO_x and ZrO_2 an ideal bilayer combination for stable and reliable memristive devices tailored for neuromorphic computing and reduce temporal variations.[24,38,39]

In this study, we have successfully fabricated and characterized a bilayer memristor with the device structure $Si/SiO_2/Pt/NbO_x/ZrO_2/Ag$, specifically engineered for neuromorphic computing applications. By integrating an NbO_x/ZrO_2 heterostructure as the switching layer, we utilized the complementary properties of these materials to achieve superior memristive performance, including reduced operating voltages, enhanced switching stability, and reliable multi-level resistance states. Our results demonstrate that the interface between NbO_x and ZrO_2 plays a critical role in controlling the formation and rupture dynamics of conductive filaments, ultimately defining the device switching behavior and synaptic characteristics. The emergence of virtual cathodes within the bilayer structure facilitates localized filament formation, contributing to improved uniformity and reduced variability in switching events. The memristor exhibits high endurance, gradual conductance modulation, and stable retention. Additionally, precise control over multi-level switching enables multipattern memorization, an essential capability for future neuromorphic systems. Collectively, these findings advance the development of high-density, low-power memristive devices compatible with existing CMOS fabrication technologies, offering a promising route toward integrating energy-efficient, brain-inspired hardware into next-generation heterogeneous electronic systems.[17,40,41]

2. Experimental section

2.1. Device fabrication

Platinum-coated substrates were initially cleaned by ultrasonic agitation in distilled water at 50 °C for 10 minutes, followed by

sequential sonication in acetone and methanol. The substrates were then dried using a nitrogen gun to ensure a residue-free surface, as shown in Fig. S1. Thin films of niobium oxide (NbO_x) and zirconium oxide (ZrO_2) were deposited *via* radio-frequency (RF) sputtering. For the NbO_x layer, a 3-inch niobium metal target was reactively sputtered in an argon–oxygen ($Ar : O_2$) environment with a gas flow ratio (sccm) of 14 : 4. The deposition was carried out at a substrate temperature of 500 °C for 35 minutes. The RF power was maintained under a base pressure of 1.6 μTorr and a working pressure of 27 mTorr to promote oxide formation. Similarly, the ZrO_2 layer was deposited using a 3-inch zirconium metal target in an $Ar : O_2$ atmosphere with a flow rate (sccm) of 10 : 10. The substrate temperature was kept at 500 °C for 1 hour, with RF sputtering performed under a base pressure of 2 μTorr and a working pressure of 26 mTorr. Post-deposition, both films were annealed at 500 °C for 30 minutes in argon, with a ramp rate of 10 °C min^{-1}, followed by natural cooling to room temperature. Silver (Ag) top electrodes with a thickness of 150 nm were deposited by thermal evaporation through a shadow mask, forming circular electrode pads with a nominal diameter of 100 μm.

2.2. Device characterization

The structural and morphological characteristics of the bilayer memristor devices were systematically investigated using advanced microscopy and spectroscopy techniques. High-resolution transmission electron microscopy (HR-TEM) was employed to visualize the layer architecture, allowing precise evaluation of thickness uniformity and interfaces. Elemental mapping through energy-dispersive X-ray spectroscopy (EDS) verified the spatial distribution of constituent elements within the device stack. Atomic force microscopy (AFM) provided insight into the surface topography and roughness variations, while X-ray photoelectron spectroscopy (XPS) was employed to analyze the chemical composition and oxidation states of the constituent layers, offering crucial information on interfacial chemistry and stoichiometry.

2.3. Electrical measurements and simulations

Electrical characterization of the bilayer memristor devices was carried out using a semiconductor parameter analyzer B1500A connected to a probe station under ambient conditions. Direct current (DC) *I–V* measurements were obtained by sweeping the bias across the top electrode while grounding the bottom electrode, with a compliance current applied to prevent permanent device damage. Synaptic functionalities such as potentiation and depression were examined through pulse-driven measurements using a waveform generator/fast measurement unit (WGFMU), where sequences of voltage pulses were applied and the corresponding conductance changes were recorded in real time. In addition, retention and endurance tests were performed at a low read voltage to evaluate the stability of resistive states over time and repeated switching cycles, ensuring reliable device operation for memory and neuromorphic applications.

Neural network simulations were carried out to examine the bilayer memristor devices for neuromorphic computing applications. The Fashion-MNIST dataset was used as the input set for image classification. The experimentally obtained conductance states of the devices were directly mapped to synaptic weights in an artificial neural network framework. Potentiation and depression characteristics were implemented as weight update rules, incorporating the non-linear and asymmetric behavior of the memristor into the training process. This methodology enabled a realistic assessment of device performance at the system level, providing insight into the influence of switching dynamics on network learning and recognition tasks.

3. Results and discussion

3.1. Structural analysis

The morphology and interfacial characteristics of the $Pt/NbO_x/ZrO_2/Ag$ bilayer stack were investigated through cross-sectional TEM and HRTEM, complemented by EDS elemental mapping and AFM to verify surface and interface quality. The cross-sectional TEM image distinctly illustrates the sequential stacking of the $Pt/NbO_x/ZrO_2/Ag$ bilayer structure with uniform thickness and continuous coverage across the entire device, as shown in Fig. 1(a). This confirms that the fabrication process successfully produced a well-defined multilayer stack without noticeable voids, discontinuities and delamination, all of which are critical for ensuring stable resistive switching performance. High-resolution TEM further reveals well-defined interfaces between the constituent layers, where NbO_x and ZrO_2 appear predominantly amorphous, while the Pt bottom electrode exhibits clear crystalline fringes corresponding to the periodic lattice planes of crystalline Pt, which provide a stable structural reference for distinguishing the amorphous oxide layers and assessing interfacial continuity, as shown in Fig. 1(b). The absence of visible interdiffusion between NbO_x and ZrO_2 indicates strong chemical confinement at the bilayer junction, ensuring that each oxide layer retains its intended role: NbO_x functioning as an oxygen-vacancy reservoir to support filament nucleation and ZrO_2 serving as a robust ion-blocking barrier that regulates filament penetration. The presence of a clearly defined NbO_x/ZrO_2 interface plays a critical role in confining conductive filament formation by creating a localized discontinuity in oxygen-vacancy concentration and electric-field distribution. This interfacial contrast preferentially anchors filament nucleation within the NbO_x layer while suppressing uncontrolled lateral filament growth into the ZrO_2 layer, thereby stabilizing filament evolution during repeated SET/RESET operations and resulting in improved switching uniformity and endurance. AFM topography (2D and 3D) provided complementary information on the surface morphology. The NbO_x film exhibited a root-mean-square roughness (R_q) of 1.204 nm and an average roughness (R_a) of 0.955 nm, while the ZrO_2 layer showed slightly higher values (R_q = 1.405 nm; R_a = 1.109 nm) which are characteristic of its denser microstructure as shown in Fig. 1 (c). Both surfaces remain within the sub-2 nm range, confirming smooth and uniform growth. This low roughness ensures homogeneous electric field distribution, intimate electrode contact, and suppression of uncontrolled current

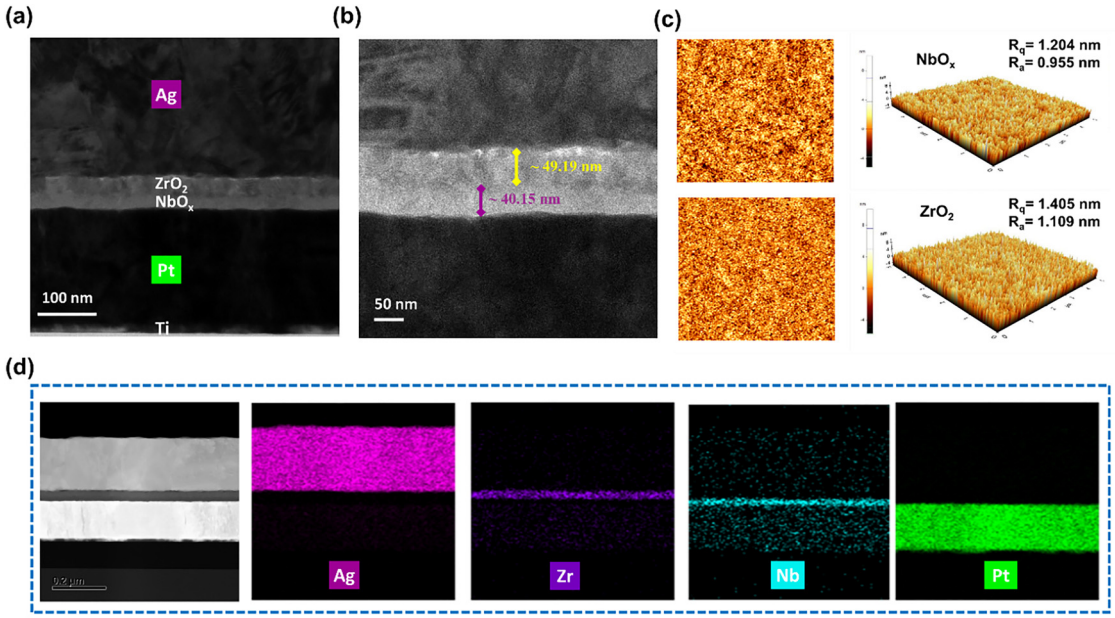

Fig. 1 Structural characterization of the Pt/NbO_x/ZrO_2/Ag bilayer device. (a) Cross-sectional TEM image confirming uniform layer stacking. (b) HRTEM image showing well-defined interfaces with predominantly amorphous oxides and crystalline Pt electrode fringes. (c) AFM topography of the NbO_x and ZrO_2 layers, showing smooth surfaces with sub-2 nm roughness. The smooth morphology and well-defined interfaces ensure uniform field distribution and reliable confinement of the conductive filaments, essential for reproducible resistive switching behavior. (d) EDS elemental mapping validating distinct distribution of Ag, Zr, Nb and Pt confirming the bilayer design.

pathways, which together play a critical role in promoting confined and reproducible filament formation during resistive switching.[42,43] AFM topography scan parameters and experimental conditions used during AFM measurements in non-contact mode are shown in Table S1. This structural integrity is further validated by EDS elemental mapping, which provides a spatially resolved distribution of Ag, Zr, Nb and Pt elements across the stack, as shown in Fig. 1(d). The distinct separation of Nb and Zr signals validates the bilayer configuration and confirms the absence of significant cation intermixing, while the uniform Ag and Pt distributions confirm complete electrode coverage. These structural analyses demonstrate that the NbO_x/ZrO_2 bilayer possesses the morphological and chemical features necessary to achieve stable and reliable memristive operation. Additional cross-sectional TEM image and the corresponding EDS elemental mapping further confirm the uniform bilayer stacking and elemental distribution, as shown in Fig. S2(a–c).

The chemical bonding environment and oxidation states in the NbO_x/ZrO_2 bilayer were systematically examined by X-ray photoelectron spectroscopy (XPS), confirming the successful formation of the bilayer stack. The O 1s spectrum of ZrO_2 deconvoluted into two main components. The dominant peak at ~529 eV corresponds to lattice oxygen (O^{2-}) bonded to Zr^{4+}. The higher binding energy peak at ~531.4 eV is assigned to surface adsorbed hydroxyl groups, oxygen vacancies and chemisorbed species which indicates the presence of surface defects and hydration, as shown in Fig. 2(a). The Zr 3d core-level XPS spectrum displays two distinct peaks at ~181.7 eV and ~184.1 eV, assigned to the Zr $3d_{5/2}$ and Zr $3d_{3/2}$ components, respectively.[44,45] This characteristic doublet with a spin–orbit splitting is consistent with the Zr^{4+} oxidation state in ZrO_2, as shown in Fig. 2(b). The XPS spectrum of the C 1s peak, originating from the surface adventitious carbon for both materials, is provided in Fig. S3(a). The symmetric peak shape and lack of additional features suggest a chemically stable and stoichiometric zirconium oxide surface without significant sub-oxide and metallic zirconium contributions. The survey spectrum of the ZrO_2 film exhibits the characteristic peaks of Zr and O, with strong signals at ~182 eV corresponding to Zr 3d and a dominant O 1s peak around ~530 eV, confirming the stoichiometric oxide nature. Additional peaks such as Zr 4p (~330 eV), Zr 4s (~230 eV) and Auger features (Zr MNN around ~990 eV) are also observed, further validating the formation of ZrO_2 as shown in Fig. 2(c). The weak C 1s peak at ~285 eV arises from adventitious carbon contamination, which is common in surface-exposed films. The absence of any extraneous impurity-related peaks confirms that the ZrO_2 layer is chemically pure and suitable as a stable dielectric barrier in the bilayer stack.[46,47] The XPS spectrum of the Nb 3d core level for the Nb-based oxide film is shown in Fig. 2(d and e). The spectrum reveals two distinct peaks at ~206.9 eV and ~209.7 eV, corresponding to the Nb $3d_{5/2}$ and Nb $3d_{3/2}$ spin–orbit components, respectively. The observed spin–orbit splitting is consistent with the Nb^{5+} oxidation state, indicating the presence of Nb_2O_5 as the predominant surface phase.[48]

The survey spectrum of the NbO_x film shows well-defined Nb 3d peaks at ~207 eV (Nb $3d_{5/2}$) and ~210 eV (Nb $3d_{3/2}$), characteristic of Nb^{5+} and Nb^{4+} oxidation states, alongside a strong O 1s peak at ~530 eV. Other signals such as Nb 4p (~365 eV), Nb 4s (~270 eV), and Auger Nb MNN transitions

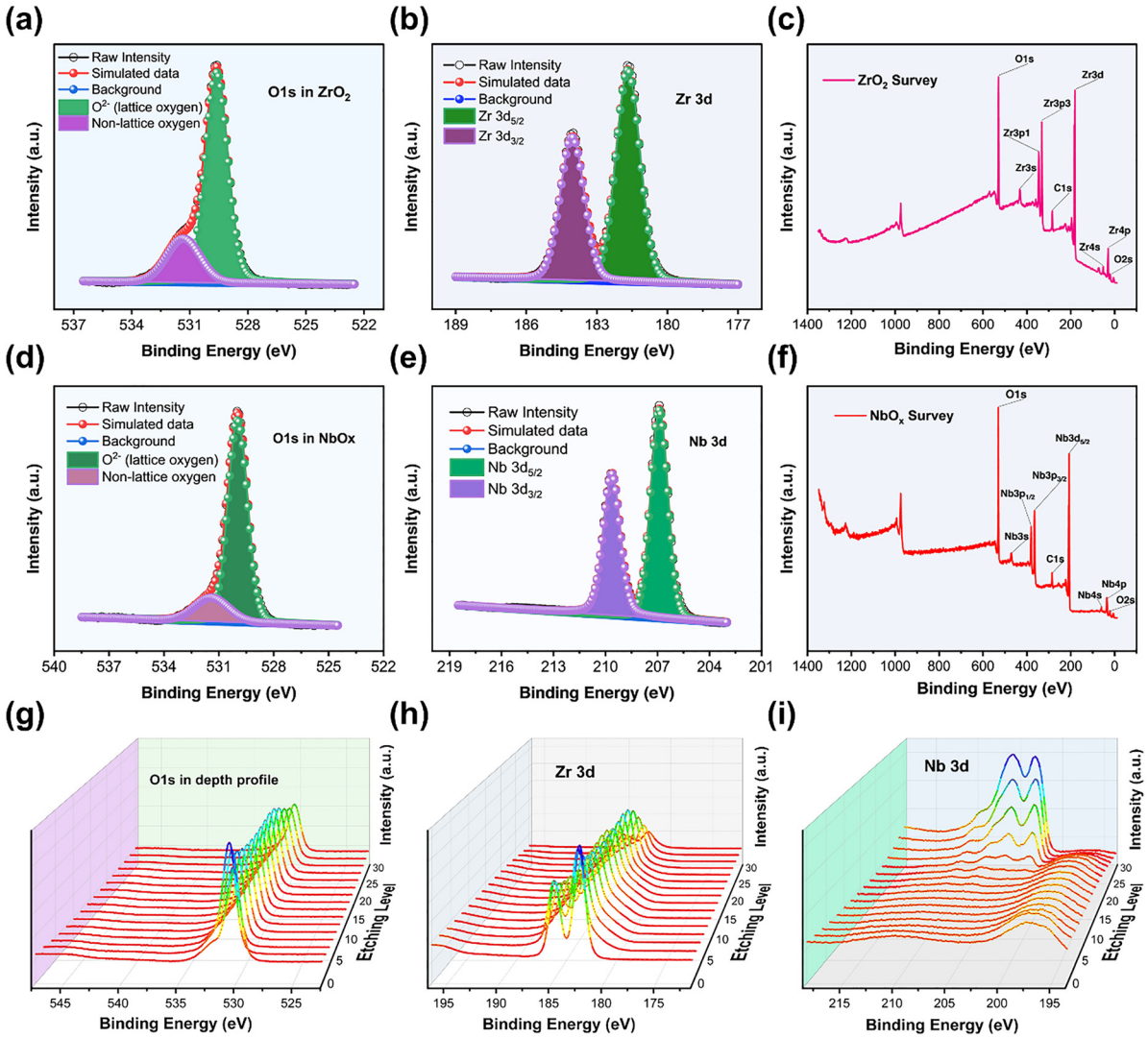

Fig. 2 XPS analysis of the NbO_x/ZrO_2 bilayer films. (a) and (d) High-resolution O 1s spectra showing lattice oxygen and oxygen-vacancy-related non-lattice oxygen components for ZrO_2 and NbO_x, respectively. (b) Zr 3d spectrum confirming Zr^{4+} in ZrO_2. (c) and (f) Survey spectra of ZrO_2 and NbO_x, showing the absence of unwanted impurities. (e) Nb 3d spectrum revealing mixed Nb^{5+}/Nb^{4+} states indicative of oxygen deficiency in NbO_x. (g)–(i) Depth profile spectra of O 1s, Zr 3d, and Nb 3d, confirming chemical stability across the thickness and distinct separation of NbO_x and ZrO_2 layers. The presence of controlled oxygen vacancies in NbO_x and stable ZrO_2 stoichiometry validates the bilayer role in providing both an active defect reservoir and a reliable barrier layer for resistive switching.

(~990 eV) are also detected, consistent with the expected Nb–O bonding environment as shown in Fig. 2(f). A small C 1s peak (~285 eV) is attributed to surface carbon contamination. Importantly, no additional impurity peaks are observed, confirming that the deposited NbO_x is chemically clean and oxygen-deficient in nature. This oxygen deficiency is directly linked to the presence of oxygen vacancies, which play a central role as active sites for resistive switching in the memristor device.[49]

Depth profile spectra further demonstrate the stability of these chemical states across the film thickness, with no evidence of significant intermixing between NbO_x and ZrO_2 as shown in Fig. 2(g–i). The coexistence of lattice and non-lattice oxygen, together with well-defined Zr^{4+} and Nb^{5+}/Nb^{4+} states, confirms the bilayer's designed functionality, in which ZrO_2 provides a robust barrier while NbO_x supplies active defects to facilitate filamentary conduction. The complete survey spectra of the depth profile is shown in Fig. S3(b).

3.2. Electrical characteristics

The electrical characteristics of the $Pt/NbO_x/ZrO_2/Ag$ bilayer memristor were systematically investigated to evaluate its resistive switching performance. The optical micrograph of the device array confirms the uniform fabrication and deposition of Ag top electrodes on the substrates, as shown in Fig. 3(a). The *I–V* cycles show stable bipolar switching, with a sharp SET transition under a positive bias and RESET under a negative bias, both occurring at low operating voltages below ±0.5 V as shown in Fig. 3(b). This low-voltage switching originates from the NbO_x layer, which facilitates easy filament formation, while the ZrO_2 barrier effectively confines the filament, leading to

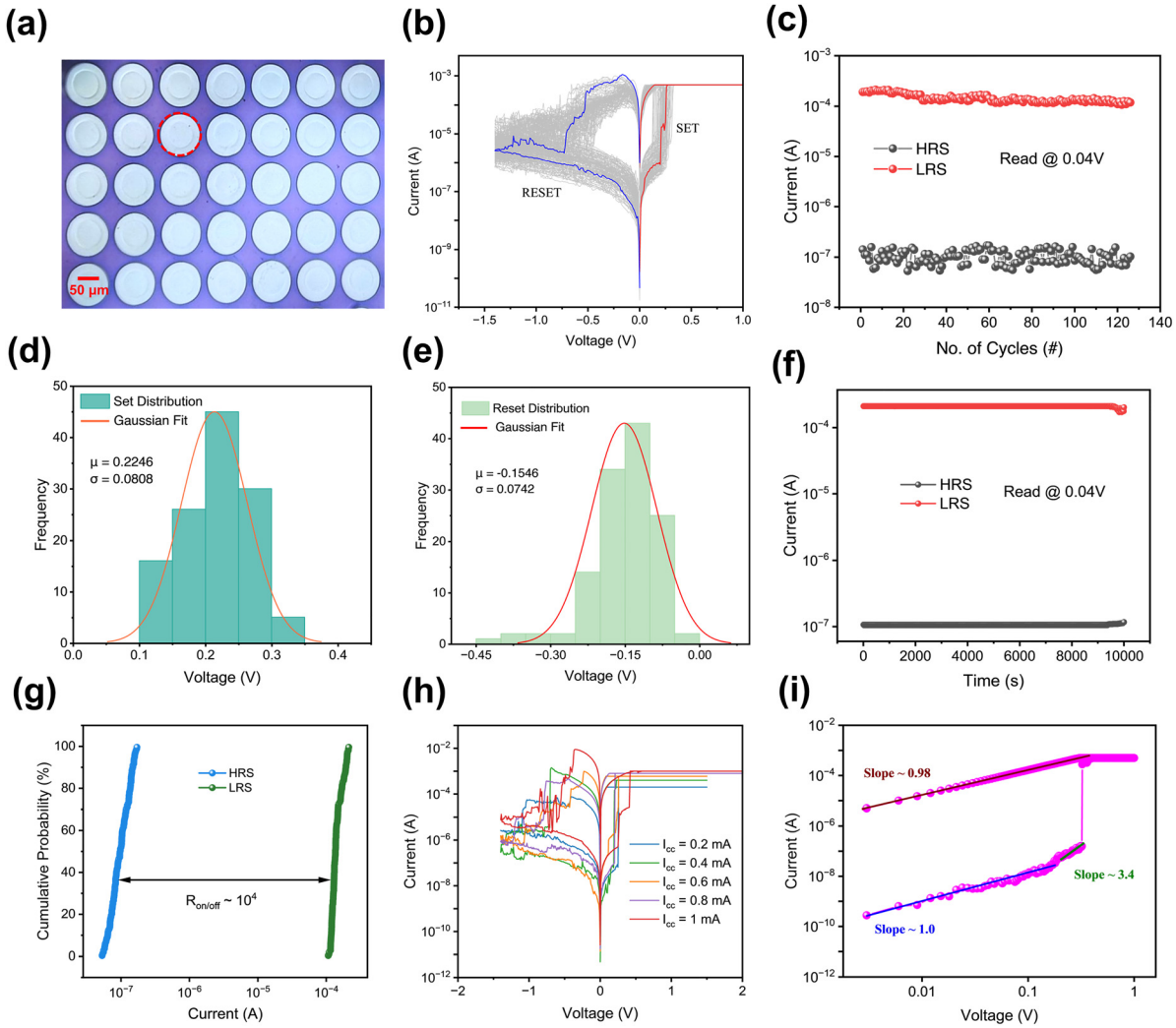

Fig. 3 Electrical characteristics of the Pt/NbO_x/ZrO_2/Ag bilayer structure. (a) Optical image of the device array confirming uniform fabrication and deposition of Ag top electrodes. (b) *I*–*V* cycles showing stable bipolar switching at low voltages with sharp set and reset transitions. (c) Endurance performance over 120 cycles, maintaining distinct and stable HRS and LRS states at a read voltage of 0.04 V. (d) and (e) Statistical distribution of the set and reset voltages fitted with Gaussian curves, revealing narrow deviations and high switching uniformity. (f) Retention characteristics demonstrated stable HRS and LRS states over 10^4 s without degradation. (g) Cumulative probability highlights the large ON/OFF ratio and uniform switching. (h) Multilevel resistive switching achieved by tuning the compliance current, enabling intermediate states beyond binary switching. (i) Conduction mechanism analysis log*I*–*V* fitting indicates ohmic conduction at low bias and trap-controlled SCLC at higher bias, consistent with vacancy-mediated filament dynamics.

reproducible cycles.[50] The device exhibits robust endurance over more than 120 cycles, where distinct and stable HRS and LRS values are maintained at a read voltage of 0.04 V as shown in Fig. 3(c). This reliable stability arises from the bilayer structure, where the well-defined interface and complementary functionalities of the two oxides confine filament formation and suppress random defect migration, together providing controlled defect modulation. This cooperative mechanism minimizes stochastic fluctuations in conductive path formation, leading to uniform switching and well-separated resistance states across cycles. For comparison, single-layer ZrO_2 and NbO_x for (>10 devices) exhibited pronounced variability in their switching parameters and unstable resistance states (Fig. S4 and S5). In contrast, the bilayer devices (>10 devices) demonstrate improved uniformity and stable switching behavior, underscoring the importance of the bilayer configuration in achieving reliable resistive switching (Fig. S6).[51]

Statistical analysis further highlights the uniformity of the device. The Gaussian-fitted set voltage distribution is centered at +0.22 V with a narrow standard deviation of 0.08, while the reset distribution is centered at −0.15 V with a deviation of 0.0742, as shown in Fig. 3(d and e). The slightly broader reset spread is due to the stochastic nature of filament rupture, though the ZrO_2 layer mitigates excessive variability by confining the rupture location. Long-term retention characteristics confirm the non-volatile nature of the device, with both HRS and LRS remaining stable for 10^4 s without noticeable degradation, as shown in Fig. 3(f). This stability arises from strong

oxygen-vacancy pinning in NbO_x and suppression of back-diffusion by the dense ZrO_2 barrier. The NbO_x layer provides a stable reservoir for defects, while the ZrO_2 layer acts as a blocking barrier that suppresses ion diffusion and random filament dissolution. This combination prevents unwanted relaxation of the conductive path and maintains distinct HRS/LRS states over extended timescales. The cumulative probability shows an ON/OFF ratio of $\sim 10^4$, which ensures a reliable memory window and reinforces the device's uniform switching behavior as shown in Fig. 3(g). This substantial separation between HRS and LRS is attributed to the bilayer architecture, where well-defined and chemically stable interface between the two oxides confines local electric fields and suppresses stochastic vacancy migration, thereby stabilizing filament formation and rupture. This physical confinement minimizes overlap between the conductive and insulating states, resulting in a wide resistance margin and enhanced switching uniformity.

Multilevel capability is demonstrated by tuning the compliance current during the set process, as shown in Fig. 3(h). Increasing the compliance current gradually reduces the LRS resistance, enabling distinct multilevel states. This behavior originates from the controlled modulation of conductive filament dimensions; the NbO_x layer, acts as a reservoir that provides mobile defects for filament growth, while the ZrO_2 layer serves as a robust barrier that confines the filament laterally and prevents uncontrolled expansion. The resulting fine control over filament thickness and conductivity allows the device to reproducibly access intermediate resistance states beyond the conventional binary HRS and LRS. These multilevel states are highly significant as they emulate the analog weight modulation of biological synapses. Instead of a simple 0 and 1, the device represents a continuum of synaptic weights, which is essential for implementing and tuning plasticity and for achieving high-density vector–matrix multiplication in neural networks. The gradual, compliance-driven tuning of conductance provides a hardware-embedded mechanism to encode multiple weight levels in a single cell, thus enabling more energy-efficient training and inference. Furthermore, the stability of these intermediate states ensures reliable retention of learned weights, addressing one of the key challenges in neuromorphic hardware. The multilevel resistive switching in the $Pt/NbO_x/ZrO_2/Ag$ bilayer memristor not only validates its applicability as a non-volatile memory element but also underscores its potential as an artificial synapse for brain-inspired computing architecture.

The conduction mechanism of the $Pt/NbO_x/ZrO_2/Ag$ bilayer device was further analyzed to understand its relation to resistive switching and neuromorphic behavior. Log *I–V* fitting indicates that, at low bias, the current follows an ohmic conduction regime with a slope ≈ 1, consistent with free electron transport through pre-existing conduction paths as shown in Fig. 3(i). At higher bias, the slope increases to ≈ 3.4, characteristic of trap-controlled space-charge-limited conduction (SCLC). This transition reflects the progressive filling of oxygen-vacancy-related trap states within NbO_x, which directly governs filament formation and dissolution.[52–54]

The resistive switching mechanism of the $Pt/NbO_x/ZrO_2/Ag$ bilayer device is illustrated in Fig. 4. In the as-deposited state, the NbO_x layer contains abundant oxygen vacancies, while the ZrO_2 layer remains stoichiometric, providing a stable dielectric barrier as shown in Fig. 4(a). Upon applying a sufficiently high forming voltage, Ag^+ ions from the top electrode and oxygen ions migrate under the electric field, initiating the creation of a conductive path through the NbO_x layer and partially penetrating the ZrO_2 barrier. This electroforming step corresponds to the abrupt current increase observed in the *I–V* characteristics, establishing the initial conductive filament as shown in Fig. 4(b). During subsequent switching cycles, the device exhibits reversible bipolar switching between HRS and LRS. In the reset process, the application of reverse bias drives Ag^+ ions back toward the top electrode and partially re-oxidizes oxygen vacancies, rupturing the conductive filament and returning the device to HRS as shown in Fig. 4(c). In contrast, during the set process, a forward bias facilitates the drift of Ag^+ and oxygen vacancies toward the interface, reestablishing a continuous filament across the NbO_x/ZrO_2 bilayer, leading to the sharp current increase as evident in the *I–V* curve as shown in Fig. 4(d). The integration of NbO_x and ZrO_2 plays a synergistic role in this switching mechanism. The NbO_x layer acts as a defect reservoir, enabling facile filament nucleation, while the ZrO_2 barrier confines filament growth, preventing uncontrolled spreading and enhancing reproducibility. This mechanism explains the low-voltage operation, stable switching windows and high ON/OFF ratio observed in the electrical characterization, further validating the bilayer design for reliable resistive switching.

3.3 Artificial synapse emulation and neuromorphic integration

The ever-increasing demand for energy-efficient and parallel data processing in artificial intelligence has exposed the limitations of conventional von Neumann computing architectures, which suffer from high power consumption and memory bottlenecks. In contrast, the human brain performs highly complex tasks at ultra-low power by utilizing massively parallel connections of neurons and synapses. Each synapse functions as a dynamic analog connection, adjusting its weight in response to the frequency and timing of neural spikes, thereby enabling adaptive learning and memory retention. Inspired by this remarkable biological efficiency, neuromorphic computing aims to replicate brain-like processing in hardware. Biological neurons consist of dendrites, axons, and synapses, where neurotransmitters mediate communication across the synaptic cleft between pre- and post-synaptic neurons. This process governs learning and memory in the brain through modulation of synaptic strength. Inspired by this mechanism, neuromorphic models emulate signal transmission using equivalent circuit elements such as synaptic conductance (G_{syn}), membrane capacitance (C_{mem}), and ionic channels (G_{Na} and G_K) to replicate excitatory and inhibitory responses. At the hardware level, memristor-based devices mimic synaptic plasticity through controllable SET and RESET processes, enabling

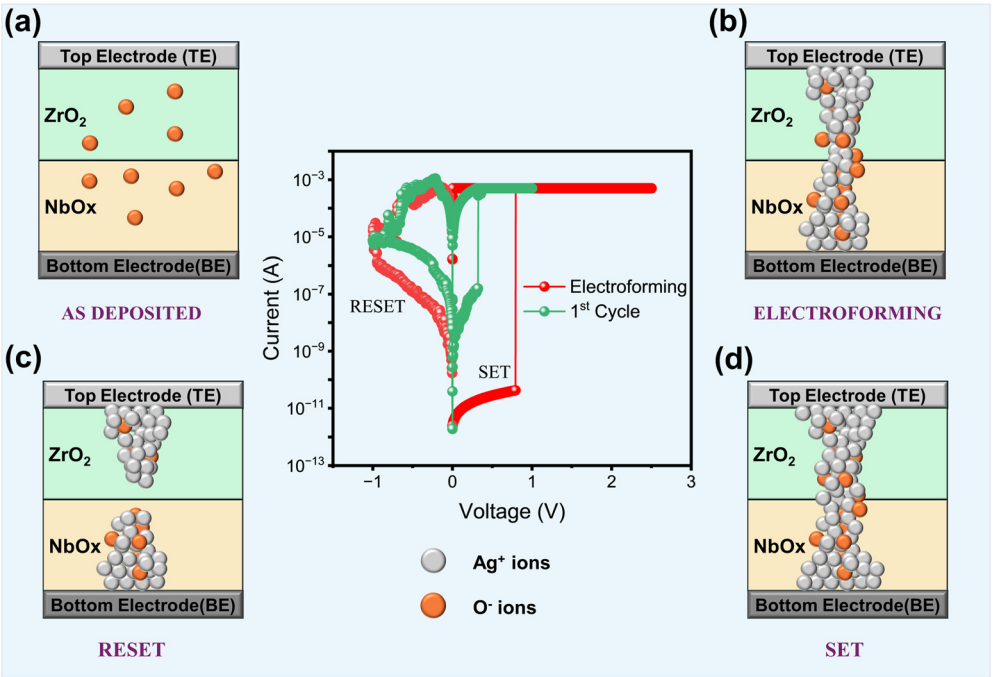

Fig. 4 Resistive switching mechanism of the Pt/NbO_x/ZrO_2/Ag bilayer device. (a) As-deposited state showing uniformly distributed oxygen vacancies in NbO_x and stoichiometric ZrO_2. (b) Electroforming process under high bias, where Ag^+ ions migrate to initiate the first conductive filament, corresponding to the abrupt current rise in the *I*–*V* curve. (c) RESET process, where reverse bias drives Ag^+ ions back and ruptures the conductive filament, restoring the high resistance state. (d) SET process, where forward bias re-establishes the filament through vacancy and Ag^+ migration, yielding the low resistance state. The central *I*–*V* curve displays the forming step (red) and first switching cycle (green), consistent with the illustrated mechanism.

the dynamic adjustment of conductance states analogous to biological synaptic weights, as shown in Fig. 5.

Memristors, with their intrinsic capability to store and modulate conductance in a nonvolatile manner, are widely regarded as promising artificial synapses for next-generation neuromorphic platforms. When an action potential arrives at the presynaptic terminal, it triggers the release of neurotransmitters into the synaptic cleft. These neurotransmitters then bind to receptors on the postsynaptic neuron, modulating the synaptic weight and thereby altering the strength of the transmitted signal. This weight modulation, known as synaptic plasticity, underlies the fundamental processes of learning and memory in biological neural networks. Short-term plasticity (STP) enables transient signal enhancement such as paired-pulse facilitation (PPF), while long-term potentiation (LTP) and depression (LTD) provide stable learning and memory retention.

The Pt/NbO_x/ZrO_2/Ag bilayer memristor investigated in this work demonstrates synaptic plasticity behaviors, closely mimicking biological learning processes. Under repeated voltage pulses, the device exhibits gradual and reproducible conductance changes, corresponding to long-term potentiation (LTP) and long-term depression (LTD) as shown in Fig. 6(a). The gradual change in conductance under consecutive pulses shows the device's ability to emulate long-term synaptic plasticity. The controlled filament formation (set) and rupture (reset) within the bilayer structure enable reproducible analog weight updates.[55,56] The LTP and LTD at different pulse voltages are provided in Fig. S7 and S8. While the overall potentiation and depression trends are maintained, higher pulse amplitudes lead to relatively faster conductance changes, consistent with the voltage-driven nature of filament dynamics. The conductance modulation exhibits a gradual and monotonic evolution with pulse number, indicating quasi-linear weight update behavior with limited nonlinearity over the accessible conductance range. This behavior is attributed to the controlled and progressive modulation of the conductive filament enabled by the NbO_x/ZrO_2 bilayer interface. These results confirm the robust and reproducible plasticity of the bilayer device under diverse operating conditions. Synaptic strength, in biological neurons or artificial devices, is often governed by an exponential dependence on repeated stimulation. In our memristor, this behavior is captured through the conductance variation with pulse application, formulated as

$$G(p) = G_{\min} + (G_{\max} - G_{\min})[1 - e^{-p/A}]$$

where $G_{\min}$ and $G_{\max}$ correspond to the lower and upper conductance limits of the device, p indicates the applied number of potentiation or depression pulses, and A represents the characteristic constant distinct for each process and derived from experimental data.

The rapid decay of the facilitation index reflects short-term synaptic plasticity, originating from the transient formation and partial relaxation of Ag conductive filaments under pulsed stimulation. This behavior is further modulated by local electric-field enhancement at the NbO_x/ZrO_2 interface and transient charge trapping effects, which influence filament

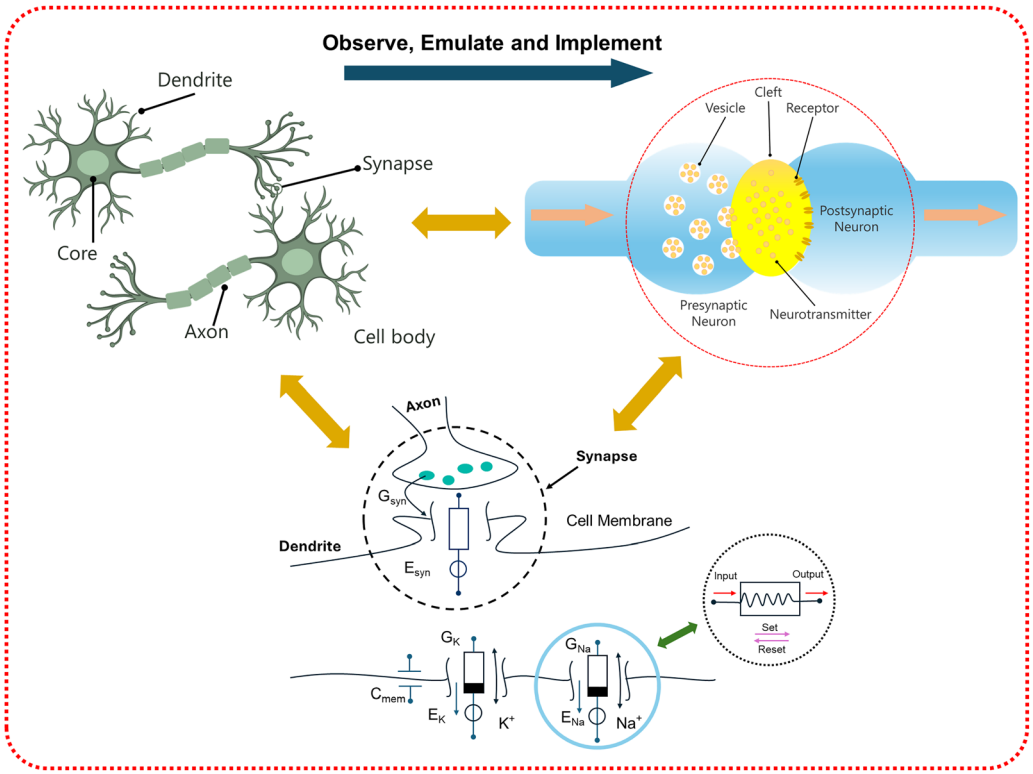

Fig. 5 Schematic illustration of the correlation between biological and artificial synaptic systems. (Top left) A biological neuron network, where dendrites and axons are interconnected through synapses. (Top right) The enlarged synapse region shows neurotransmitter release from presynaptic vesicles across the synaptic cleft, binding to postsynaptic receptors to enable signal transmission. (Bottom) Equivalent circuit representation of neural signaling, including synaptic conductance (G_{syn}), membrane capacitance (C_{mem}), and potassium (K^+) and sodium (Na^+) ion channels with their corresponding equilibrium potentials (E_K, E_{Na}). The analogy to a memristor-based artificial synapse is illustrated, where the SET and RESET states mimic synaptic potentiation and depression, enabling neuromorphic computing applications.

stability. These dynamic processes emulate neurotransmitter release and depletion in biological synapses, demonstrating the device's capability to reproduce short-term synaptic responses, as shown in Fig. 6(b). The measured PPF index decays exponentially with increasing pulse interval, in close agreement with biological short-term plasticity, further validating the device's ability to reproduce fundamental neuronal dynamics.

The symmetric modulation of conductance with respect to normalized pulses highlights the device's ability to achieve balanced potentiation and depression. The ZrO_2 layer suppresses the stochastic fluctuations in vacancy migration, while NbO_x provides a controlled defect reservoir, resulting in linear-like conductance tuning as shown in Fig. 6(c and e). This suppresses weight drift and ensures stable multilevel states across cycles.

The network simulation with Fashion-MNIST input shows that the memristor-based synapses store and process analog weights effectively. The high recognition probability (probability $\sim$0.80) stems from stable and gradual conductance modulation, which allows the network to distinguish subtle pixel variations. The bilayer's controlled filamentary dynamics prevent abrupt switching and enable analog-like behavior rather than binary operation as shown in Fig. 6(d). The comparison between baseline and memristor models shows that while the memristor-based network converges slightly slower due to hardware non-idealities (nonlinearity and variability), it still reaches high accuracy. Fig. S9 illustrates the overall mechanism of the neuromorphic simulation, where experimental pulse data are preprocessed, fitted to learning rules and mapped to synaptic weights for neural network training, validation, and performance evaluation. This is because the large ON/OFF ratio ($\sim 10^4$) and stable intermediate states reduce overlap between weights, ensuring sufficient precision for vector–matrix multiplication, as shown in Fig. 6(f). The diagonal dominance in the confusion matrix indicates that most classes are accurately recognized. The occurrence of classification errors are minimized because the memristor's analog weight states are reproducible, enabling consistent mapping of input features to correct classes. This stability arises from the confined vacancy dynamics at the NbO_x/ZrO_2 interface, which reduces random conductance fluctuations that typically degrade classification accuracy as shown in Fig. 6(g).

These results highlight the effectiveness of the bilayer design in providing stable, tunable and reproducible synaptic weights. The $Pt/NbO_x/ZrO_2/Ag$ memristor not only demonstrates low-voltage operation, robust endurance and long retention, but also exhibits reliable multilevel states and neuromorphic functions such as potentiation, depression,

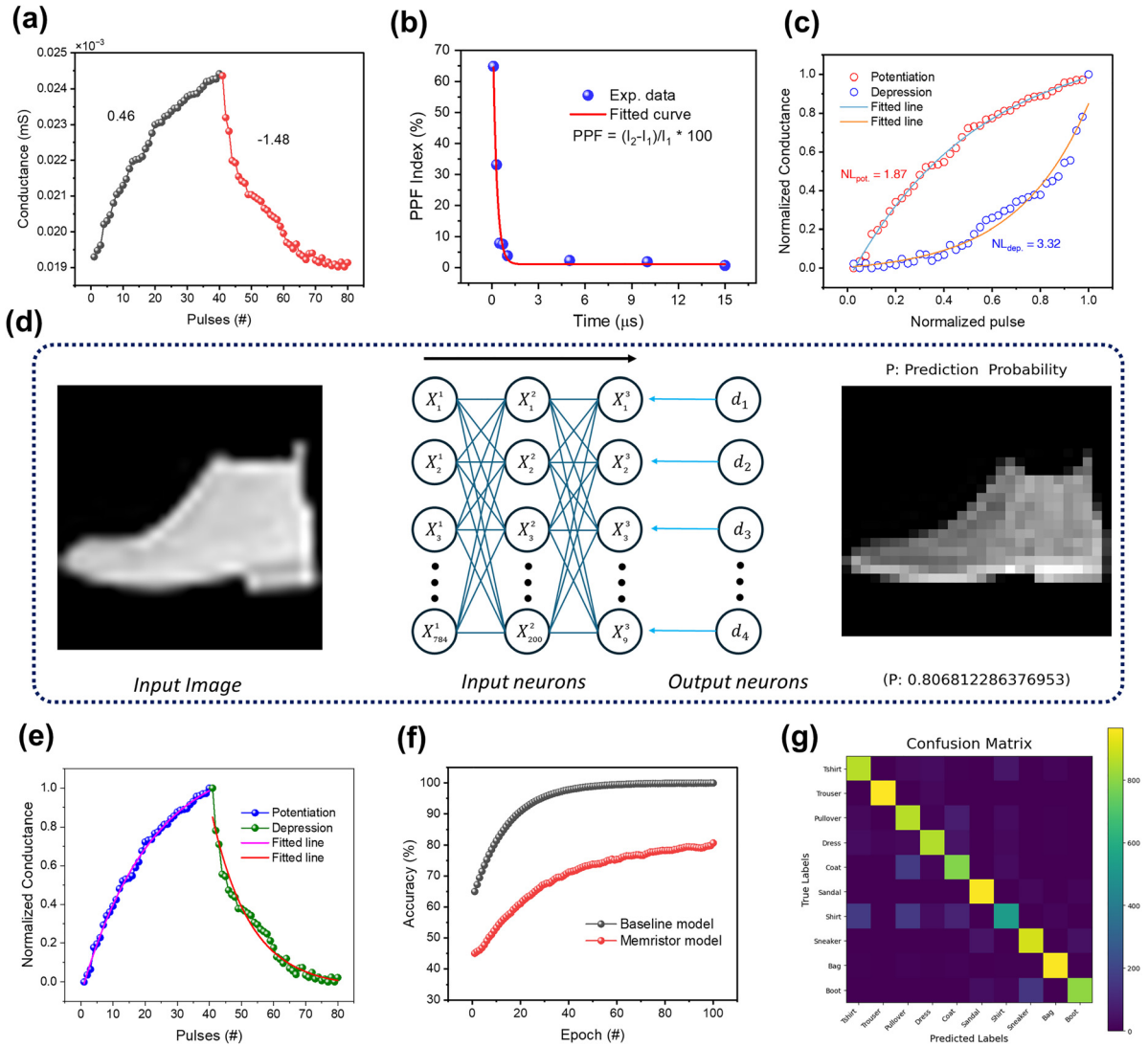

Fig. 6 Synaptic and neuromorphic characteristics of the Pt/NbO_x/ZrO_2/Ag bilayer memristor. (a) Potentiation and depression characteristics under consecutive voltage pulses of (+0.46 V and −1.48 V), showing gradual and repeatable conductance modulation. (b) Paired-pulse facilitation (PPF) response of the bilayer device. (c) Normalized conductance *versus* normalized pulse number, highlighting symmetric and controllable weight modulation suitable for neuromorphic learning with non-linearity of 1.87 and 3.32 for potentiation and depression, respectively. (d) An artificial neural network (ANN) schematic illustrates the classification process for the Fashion-MNIST dataset, where input images are mapped to weighted synaptic connections and processed through output neurons for recognition. (e) Normalized conductance *versus* pulses with fitted line parameters. (f) Training accuracy comparison highlights the effective convergence and learning capabilities. (g) Confusion matrix of F-MNIST classes validates the classification performance.

and paired-pulse facilitation. The device further achieves high recognition accuracy on the Fashion-MNIST dataset, validating its capability for practical neuromorphic computing applications. Table S2 provides a comparison with recently reported memristive devices, highlighting key metrics such as the switching voltage, switching type, neural network performance and key summary of work.

4. Conclusions

In summary, we have demonstrated the successful fabrication and characterization of a Pt/NbO_x/ZrO_2/Ag bilayer memristor, which exhibits low-voltage, reliable and reproducible resistive switching. Structural analyses confirmed the presence of a well-defined interface, smooth morphology, and distinct chemical partitioning between the NbO_x and ZrO_2 layers, which together provide a stable platform for controlled filament formation. Electrical characterization revealed excellent endurance, long retention, narrow switching variability and a high ON/OFF ratio exceeding 10^4 s. The device further demonstrated multilevel conductance states through compliance current modulation and conduction mechanisms consistent with Ag filamentary switching, enabling both short-term and long-term synaptic plasticity. Importantly, neuromorphic simulations validated its ability to mimic key synaptic functions, such as LTP, LTD and

PPF, while achieving a high classification accuracy of $\geq 80\%$ in an artificial neural network trained on F-MNIST data. These results highlight the dual role of the NbO_x/ZrO_2 bilayer; NbO_x serves as an oxygen-vacancy reservoir to lower the switching energy and ZrO_2 acts as a barrier to confine filaments and improve uniformity. Taken together, this work establishes the bilayer memristor as a promising candidate for next-generation nonvolatile memory and energy-efficient neuromorphic computing systems, bridging nanoscale material design with large-scale brain-inspired functionality.

Author contributions

Muhammad Wajid Zulfiqar: writing – original draft, writing – review & editing, conceptualization, investigation, formal analysis, validation, visualization. Sobia Nisar: validation, formal analysis, investigation, writing – review & editing. Rimsha Zulfiqar: writing – review & editing, investigation, formal analysis, validation. Muneeb Ahmad: investigation, formal analysis, data curation. Muhammad Rabeel: writing – review & editing, validation, software. Hammad Ghazanfar: software, resources, methodology. Saikh Mohammad Wabaidur: visualization, validation, formal analysis. Aamir Rasheed: visualization, methodology, investigation. Honggyun Kim: writing – review & editing, validation, software, resources. Ghulam Dastgeer: project administration, methodology, supervision, writing – original draft, writing – review & editing. Deok-kee Kim: supervision, funding acquisition, project administration.

Conflicts of interest

The authors declare no conflict of interest.

Data availability

Data will be available from the corresponding author on reasonable request.

The data supporting this article have been included as part of the supplementary information (SI). Supplementary information (SI) is available. See DOI: https://doi.org/10.1039/d5tc04061b.

Acknowledgements

This work was supported by the National Research Foundation (NRF) of Korea, funded by the Ministry of Science and ICT (RS-2024-00468995 and RS-2025-02303505). The authors would like to extend their sincere appreciation to the Ongoing Research Funding program, (ORF-2026-448), King Saud University, Riyadh, Saudi Arabia.

References

1 X. Zou, S. Xu, X. Chen, L. Yan and Y. Han, *Sci. China Inf. Sci.*, 2021, **64**, 160404.
2 H. Seok, D. Lee, S. Son, H. Choi, G. Kim and T. Kim, *Adv. Electron. Mater.*, 2024, **10**, 2300839.
3 S. Zhao, Y. Wang, M. Fei, L. Chen, Y. Wen and P. Li, *Adv. Funct. Mater.*, 2026, e21724.
4 T. Chen, S. Song and Z. Wang, IEEE Transactions on Circuits and Systems I: Regular Papers, 2025.
5 G. Dastgeer, S. Nisar, A. Rasheed, K. Akbar, V. D. Chavan, D.-K. Kim, S. M. Wabaidur, M. W. Zulfiqar and J. Eom, *Nano Energy*, 2024, **119**, 109106.
6 Z. Padamsey and N. L. Rochefort, *Curr. Opin. Neurobiol.*, 2023, **78**, 102668.
7 Z. Li, J. Jin, D. Zhang and C. Chen, *Multimed. Syst.*, 2025, **31**, 1–26.
8 Y. Huang, Q. Wu, T. Gong, J. Yang, Q. Luo and M. Liu, *Nat. Commun.*, 2025, **16**, 8063.
9 A. Mehonic and A. J. Kenyon, *Nature*, 2022, **604**, 255–260.
10 H. Tian, Z. Wang, Z. Cao and B. Sun, *Chaos, Solitons Fractals*, 2025, **201**, 117292.
11 Y. Choi, S. Jeong, H. Jeong, S. Han, J. Ko, S. E. Yu, Z. Xu, M. S. Chae, M. Son and Y. Meng, *npj Unconv. Comput.*, 2025, **2**, 8.
12 S. Dutta, S. Panchanan, J. H. Yoo, S. Kumar, H. C. Yoo, S. I. Seok, G. Dastgeer and D. H. Yoon, *Adv. Funct. Mater.*, 2024, 2410810.
13 S. Panchanan, G. Dastgeer, S. Dutta, M. Hu, S.-U. Lee, J. Im and S. I. Seok, *Matter*, 2024, 3949–3969.
14 S. Panchanan, S. Dutta, G. Dastgeer, R. Jaafreh, K. Hamad and S. I. Seok, *Adv. Funct. Mater.*, 2025, e20665.
15 Z. Li, J. Jin, D. Zhang and C. Chen, *Integration*, 2025, 102500.
16 D. Yang, W. Meng, Z. Wang, T. Yu, C. Li, Q. Zhang, Z. Zhang, H. Li, Y. Lin and F. Xue, *Nat. Commun.*, 2025, **16**, 10666.
17 M. Lanza, S. Pazos, F. Aguirre, A. Sebastian, M. Le Gallo, S. M. Alam, S. Ikegawa, J. J. Yang, E. Vianello and M.-F. Chang, *Nature*, 2025, **640**, 613–622.
18 Z. Xia, X. Sun, Z. Wang, J. Meng, B. Jin and T. Wang, *Nano-Micro Lett.*, 2025, **17**, 217.
19 Y. Wen, Y. Yang and Y. Li, *IEEE Trans. Power Electron.*, 2025, **13**, 69690–69704.
20 Y. Kim, C. W. Lee and H. W. Jang, *J. Electron. Mater.*, 2025, **54**, 3609–3650.
21 B. Sun, J. Zhang, J. Song, J. Meng, D. W. Zhang, T. Wang and L. Chen, *InfoMat*, 2025, e70044.
22 F. Yu, X. Wang, R. Guo, Z. Ying, S. Cai and J. Jin, *Integration*, 2025, 102475.
23 M. Ismail, H. Abbas, C. Choi and S. Kim, *Appl. Surf. Sci.*, 2020, **529**, 147107.
24 M. Ismail, H. Abbas, C. Choi and S. Kim, *J. Alloys Compd.*, 2020, **835**, 155256.
25 M. W. Zulfiqar, S. Nisar, G. Dastgeer, M. Rabeel, H. Ghazanfar, A. Ali, M. Imran, H. Kim and D.-K. Kim, *Nanoscale*, 2025, **17**, 17881–17918.
26 J. Park, E. Cha, D. Lee, S. Lee, J. Song, J. Park and H. Hwang, *Microelectron. Eng.*, 2015, **147**, 318–320.
27 D. Ju, H. Ji, J. Lee and S. Kim, *APL Mater.*, 2024, 12.
28 S. Dong, Q. Huang, H. Luo, S. Xiang, L. Zhao, H. Yang, L. Yu and C. Yao, *IEEE Trans. Plasma Sci.*, 2025, **53**(06), 1277–1284.

29 S. Dong, S. Xiang, L. Zhao, Q. Huang, H. Yang, H. Luo, C. Yao and L. Yu, *IEEE Trans. Instrum. Meas.*, 2025.
30 D. Panda and A. Acharya, *ChemNanoMat*, 2025, 2500158.
31 Y. He, M. Yuan, Q. Li, L. Tang, W. Yang, Y. Ping, H. He and B. Deng, *IEEE Sens. J.*, 2025, **25**(21), 39849–39857.
32 Z. Chong, C. Wang, H. Zhang and S. Zhang, *IEEE Trans. Instrum. Meas.*, 2025, **74**, 2010014.
33 J. W. Lee, L. Cai, J. S. Nam, D. Kim, T. Kim, S. Kim, J. H. Lee, C. Jang, S. Baek and J. Han, *Adv. Sci.*, 2025, e11489.
34 A. Ruiz-Caridad, G. Marcaud, E. Duran-Valdeiglesias, J. M. Ramirez, J. Zhang, C. Alonso-Ramos, X. LeRoux, L. Largeau, S. Serna and N. Dubreuil, *IEEE J. Sel. Top. Quantum Electron.*, 2021, **28**, 1–13.
35 M. Kim and R. Carpenter, *J. Electron. Mater.*, 2003, **32**, 849–854.
36 S. Kumar, J. P. Strachan and R. S. Williams, *Nature*, 2017, **548**, 318–321.
37 D. Ju and S. Kim, *Adv. Funct. Mater.*, 2024, **34**, 2409436.
38 T. Boynazarov, J. Lee, H. Lee, S. Lee, H. Chung, D. H. Ryu, H. Abbas and T. Choi, *J. Mater. Sci. Technol.*, 2025, **227**, 164–173.
39 M. Ahmad, H. Kim, I. Ahmad, H. Ghazanfar, F. Ghafoor, J. Aziz, M. Rabeel, M. Farooq Khan, M.-J. Lee, G. Dastgeer and D.-K. Kim, *Mater. Today Nano*, 2025, **32**, 100706.
40 F. Cai, J. M. Correll, S. H. Lee, Y. Lim, V. Bothra, Z. Zhang, M. P. Flynn and W. D. Lu, *Nat. Electron.*, 2019, **2**, 290–299.
41 E. Wu, Y. Wang, S. Huo, J. Xu, M. Sheng, H. Liu, L. Zhong, J. Gao, Y. Xie and C. Pan, *Adv. Funct. Mater.*, 2025, e18764.
42 J. Chen, Z. Feng, M. Luo, J. Wang, Z. Wang, Y. Gong, S. Huang, F. Qian, Y. Zhou and S.-T. Han, *J. Mater. Chem. C*, 2021, **9**, 15435–15444.
43 T. Zeng, S. Shi, K. Hu, L. Jia, B. Li, K. Sun, H. Su, Y. Gu, X. Xu and D. Song, *Adv. Mater.*, 2024, **36**, 2401021.
44 D. K. Lee, G. Noh, S. Oh, Y. Jo, E. Park, M. J. Kim, D. Y. Woo, H. Wi, Y. Jeong and H. J. Jang, *InfoMat*, 2025, **7**, e12635.
45 X. Chen, F. Wang, X. Lin, Z. Li, H. Du, Y. Luo, P. Sun, Y. Wang, Y. Han and L. Zheng, *J. Alloys Compd.*, 2025, **1014**, 178794.
46 S. Ali, M. Hussain, M. Ismail, M. W. Iqbal and S. Kim, *J. Alloys Compd.*, 2024, **997**, 174802.
47 X. Yan, C. Qin, C. Lu, J. Zhao, R. Zhao, D. Ren, Z. Zhou, H. Wang, J. Wang and L. Zhang, *ACS Appl. Mater. Interfaces*, 2019, **11**, 48029–48038.
48 Z. Dong, L. Qian, Q. Li, J. Guo, L. Wang, S. Wu, R. Xiong, Y. Liu and C. He, *Appl. Surf. Sci.*, 2025, **687**, 162295.
49 Y. Cho, J. Heo, S. Kim and S. Kim, *Surf. Interfaces*, 2023, **41**, 103273.
50 K. Jiang, H. Jung, T.-T. Pham, D. Q. Dao, T. K. A. Nguyen, H. Yu, Y. Men and E. W. Shin, *J. Alloys Compd.*, 2021, **861**, 158636.
51 K. Wang, Q. Hu, B. Gao, Q. Lin, F.-W. Zhuge, D.-Y. Zhang, L. Wang, Y.-H. He, R. H. Scheicher and H. Tong, *Mater. Horiz.*, 2021, **8**, 619–629.
52 N. K. Upadhyay, W. Sun, P. Lin, S. Joshi, R. Midya, X. Zhang, Z. Wang, H. Jiang, J. H. Yoon and M. Rao, *Adv. Electron. Mater.*, 2020, **6**, 1901411.
53 Z. Yang, X. Huang, Y. Liu, Z. Wang, Z. Zhang, B. Ma, H. Shang, L. Wang, T. Zhu and X. Duan, *Small Methods*, 2025, **9**, 2401259.
54 Y. Yang, B. Sun, S. Mao, J. Qin, M. Liu, Z. Rao, W. Lin and Y. Zhao, *Mater. Today Commun.*, 2025, **44**, 111941.
55 J. Chen, W.-Q. Pan, Y. Li, R. Kuang, Y.-H. He, C.-Y. Lin, N. Duan, G.-R. Feng, H.-X. Zheng and T.-C. Chang, *IEEE Electron Device Lett.*, 2020, **41**, 353–356.
56 Q. Wang, R. Luo, Y. Wang, W. Fang, L. Jiang, Y. Liu, R. Wang, L. Dai, J. Zhao and J. Bi, *Adv. Funct. Mater.*, 2023, **33**, 2213296.